

Low-Loss Plasmonic Dielectric Nanoresonators

Yi Yang,^{*,†} Owen D. Miller,^{*,‡} Thomas Christensen,[†] John D. Joannopoulos,[†] and Marin Soljačić[†]

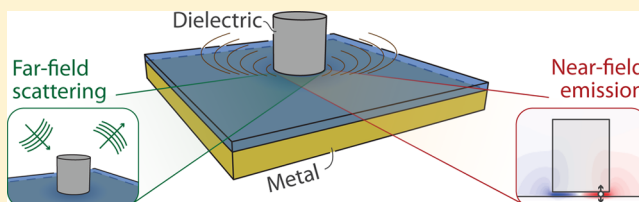
[†]Research Laboratory of Electronics, Massachusetts Institute of Technology, Cambridge, Massachusetts 02139, United States

[‡]Department of Applied Physics & Energy Sciences Institute, Yale University, New Haven, Connecticut 06520, United States

S Supporting Information

ABSTRACT: Material losses in metals are a central bottleneck in plasmonics for many applications. Here we propose and theoretically demonstrate that metal losses can be successfully mitigated with dielectric particles on metallic films, giving rise to hybrid dielectric–metal resonances. In the far field, they yield strong and efficient scattering, beyond even the theoretical limits of all-metal and all-dielectric structures. In the near field, they offer high Purcell factor (>5000), high quantum efficiency ($>90\%$), and highly directional emission at visible and infrared wavelengths. Their quality factors can be readily tailored from plasmonic-like (~ 10) to dielectric-like ($\sim 10^3$), with wide control over the individual resonant coupling to photon, plasmon, and dissipative channels. Compared with conventional plasmonic nanostructures, such resonances show robustness against detrimental nonlocal effects and provide higher field enhancement at extreme nanoscopic sizes and spacings. These hybrid resonances equip plasmonics with high efficiency, which has been the predominant goal since the field's inception.

KEYWORDS: Nanoparticles, nanoantennas, radiative efficiency, light scattering, spontaneous emission, nonlocality



The material composition of an optical nanoresonator dictates sharply contrasting properties: metallic nanoparticles^{1–6} support highly subwavelength plasmons with large field strengths but that suffer from intrinsic material losses,^{7–11} whereas dielectric nanoparticles^{12–15} support exquisite low-loss versatility but only moderate confinement as their sizes must generally be wavelength-scale or larger. In this Letter, we propose and theoretically demonstrate that a combined approach—dielectric nanoparticles on metallic films—can exhibit a unique combination of strong fields and high confinement alongside small dissipative losses. We show the utility of such hybrid plasmonic dielectric resonators for (i) far-field excitations, where subwavelength silicon-on-silver nanoparticles can scatter more efficiently than is even theoretically possible for any all-metal or all-dielectric approach, and (ii) near-field excitations, where highly directional spontaneous emission enhancements >5000 are possible with quantum efficiencies $>90\%$ and even approaching unity. Moreover, the dielectric composition of the nanoparticle, when placed atop a metallic supporting film, should mitigate much of the quantum- and surface-induced nonlocal damping that occurs at nanometer scales, an effect we confirm quantitatively with a hydrodynamic susceptibility model. Furthermore, as our approach does not rely on nanostructured metallic components, it strongly constrains parasitic dissipation arising from fabrication imperfections. More broadly, simple geometrical variations provide wide control over the individual resonant-coupling rates to photon, plasmon, and dissipative degrees of freedom, opening a pathway to low-loss, high-efficiency plasmonics.

Mitigating loss is a pivotal goal^{16–19} in plasmonics. When nanoparticles interact with plane waves, their cross sections are

typically dominated by dissipative absorption. In the near field, large spontaneous-emission enhancements (Purcell factors) have been demonstrated^{20–24} through mode-volume squeezing, but they have been typically accompanied by sub-50% quantum efficiencies at visible frequencies. In a recent paper,²⁵ we showed that optically thin films enable one to break the 50% radiative efficiency barrier in all-metal structures. A subsequent question that emerges is whether dielectric-like *near-unity* efficiency and large plasmonic confinement can be simultaneously achieved. Previously proposed hybrid structures^{26,27} with separate dielectric (director) and metal (feed) functionality exhibit better radiative efficiency, but at the cost of lower enhancements. This trade-off suggests the notion that strong and efficient plasmonic antennas are only possible at infrared frequencies,¹⁶ where they behave akin to perfect conductors and “plasmonic” effects are minor. Quantum corrections in plasmonics,^{28–31} e.g., due to electron tunneling^{32–34} and nonlocality,^{35–37} further limit the ultimate enhancement of plasmonic resonators.

The difficulty of achieving low-loss plasmons has led to the perception that high confinement is simply incompatible with low loss, as large fields near/in a metal surface may necessarily generate significant dissipation. This intuition has led to the burgeoning field of alternative plasmonic materials,^{19,38,39} whereby highly doped semiconductors or polar dielectrics ideally exhibit negative real permittivities with small imaginary (lossy) parts. There has been a complementary effort in all-

Received: February 27, 2017

Revised: April 20, 2017

Published: April 25, 2017

dielectric nanoparticles^{12–14} and metamaterials,^{14,15} but sub-wavelength resonances fundamentally require metallic components with negative permittivities.^{7,16,40} Material engineering has also been proposed in the form of band engineering⁴¹ and gain offsets.⁴² The perceived confinement–loss trade-off is rigorously correct for quasistatic plasmonic resonators,⁷ in which the desired resonant frequency directly sets the fraction of the field intensity that must reside within the lossy metal.^{7,43,44} In closed nonradiative plasmonic systems, proper geometrical optimization of dielectric–metal waveguides can reduce propagation losses;⁴⁵ in open systems, the central unanswered question is whether their radiative coupling rates can be strongly increased such that radiation significantly exceeds near-field dissipative losses. Here we show that open resonators comprising high-index, low-loss nanoparticles on metallic films can simultaneously achieve high confinement and high radiative efficiencies, without significant dissipative loss.

Conceptual Basis. We propose a hybrid dielectric–metal resonator (Figure 1a) that mitigates restrictions from metal

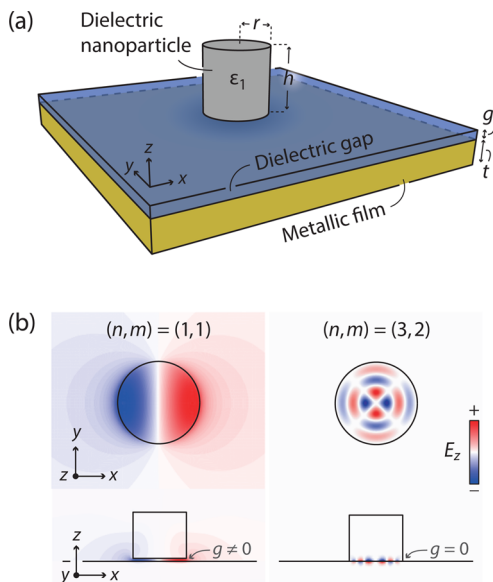


Figure 1. Hybrid dielectric–metal resonances. (a) Schematic of the structure, composed of a metallic layer of thickness t , a dielectric spacer with gap size g , and a dielectric cylindrical nanoparticle of permittivity ϵ_1 , height h , and radius r . For simplicity, we here consider vacuum as the ambient and gap media. (b) E_z mode profiles of two selected hybrid resonances, for a Si cylinder on a Ag substrate. (Material parameters are detailed in Supporting Information S1.)

losses on plasmonic scattering, emission, and quality factors to a great extent. The cylindrical symmetry implies that resonances can be labeled with indices (n, m) , enumerating field variations in the radial and azimuthal directions, respectively. Unlike the widely used all-metal “gap–plasmon” resonances^{46–50} (hereafter, metal–metal resonances), which require a nonzero gap to squeeze the field inside due to their metal-antenna-like operation,^{4,51} the dielectric–metal resonances strongly confine the resonant field for either zero or nonzero gap (Figure 1b).

Conceptually, the dielectric–metal resonances can be understood as the surface plasmons of a planar multilayer metal–dielectric system restricted to specific quantized wavevectors k_{nm} . The nanoparticle’s boundary reflects surface plasmons of general wavevector k without phase shift. For a

cylinder of radius r , the round-trip phase over the nanoparticle is given by the Bessel function of the first kind $J_n(kr)$. Localized resonances are supported when this round trip phase vanishes, i.e., at the Bessel zeros J_{nm} :

$$k_{nm}r \simeq J_{nm} \quad (1)$$

Resonant frequencies are obtained by sampling the multilayer surface plasmon dispersion curve, $\omega(k)$, at the resonant wavevectors $k_{nm} \simeq J_{nm}/r$ (Figure 2b), as verified by the agreement between analytics and numerics (Figure 2c). Equation 1 is most accurate for low-order resonances, when the plasmon reflection phase⁵² at the nanoparticle boundary is small ($\text{Re } k \gg \text{Im } k$). Equation 1 is also generalizable to other nanoparticle geometries and more complex multilayers.

This simple, yet accurate, picture of the hybrid resonances, as part-plasmon, part-Bessel resonances, illustrates the separation of key functionality: the plasmonic metal provides vertical confinement, while the dielectric provides horizontal confinement and dictates the resonant condition. External radiative coupling occurs at the low-loss dielectric–air interface, away from the lossy metal, enabling higher radiative efficiencies than those in conventional plasmonic nanostructures.

Far-Field Scattering. Metallic nanoparticles generally scatter more strongly than all-dielectric nanoparticles. Yet this large scattering strength—as measured, e.g., by the optical cross-section per unit particle volume—is typically accompanied by significant absorption. Thus, for many applications where absorption is undesirable (such as photovoltaics^{53,54}), the critical figure of merit is scattering strength accompanied by a high radiative efficiency. Here we leverage recently developed optical-response bounds to show that low-loss dielectric nanoparticles on metallic films can achieve subwavelength scattering with a large radiative efficiency, surpassing all-metal and all-dielectric scatterers and approaching fundamental limits.

There has been significant interest in finding general upper bounds to optical response,^{55,56} and recently we developed new such bounds.^{9–11} Passivity, which requires non-negative absorbed and scattered powers, imposes limits to the currents that can be excited in an absorptive scatterer, leading to bounds that are independent of shape, which account for material loss ($\propto \text{Im } \chi$, for material susceptibility χ), and which can incorporate radiative-efficiency constraints. The bounds demonstrate¹⁰ that a high radiative efficiency, defined as $\eta \equiv \sigma_{\text{sca}}/(\sigma_{\text{sca}} + \sigma_{\text{abs}}) = \sigma_{\text{sca}}/\sigma_{\text{ext}}$ (where σ_{sca} , σ_{abs} , and σ_{ext} are the scattering, absorption, and extinction cross sections, respectively), necessarily reduces the largest cross-section per volume that can be achieved. A natural figure of merit (FOM_{sca}) emerges: $\sigma_{\text{sca}}/V \times 1/[\eta(1 - \eta)]$ (equivalently, $\sigma_{\text{ext}}/\sigma_{\text{abs}} \times \sigma_{\text{ext}}/V$), which rewards high scattering cross-section (σ_{sca}/V) as well as a high radiative efficiency ($\eta \gg 0.5$). The FOM_{sca} is subject to the bound¹⁰

$$\text{FOM}_{\text{sca}} \equiv \frac{\sigma_{\text{sca}}/V}{\eta(1 - \eta)} \leq \frac{\omega}{c} \frac{|\chi(\omega)|^2}{\text{Im } \chi(\omega)} \frac{I_{\text{inc}}}{I_0} \quad (2)$$

which depends only on the frequency ω , the material composition, and the incident field properties. I_{inc}/I_0 is the ratio of the incident-field intensity I_{inc} (including, e.g., reflection from a planar film in the absence of the nanoparticle) integrated over particle volume to the intensity of the plane wave. Perfect radiative efficiency ($\eta = 1$) is unachievable for lossy scatterers, such that eq 2 cannot diverge. Equation 2 clearly shows that low-loss materials offer the possibility for

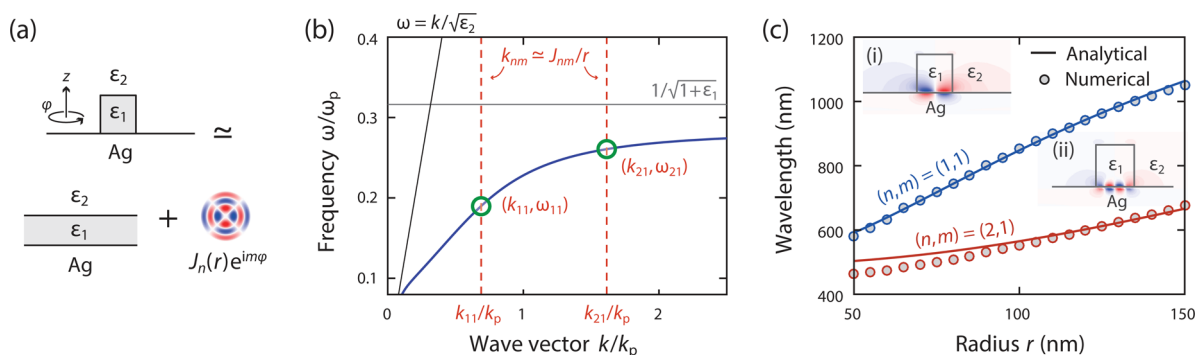


Figure 2. Analytical model of hybrid dielectric–metal resonances. (a) Pictorial representation of the hybrid resonance, which approximately satisfies a Bessel-function phase-matching condition, eq 1, imposed on the underlying planar structure. (b) Application of eq 1 illustrated in a concrete system ($h = 100$ nm, with $\epsilon_1 = 12.25$, $\epsilon_2 = 1$, $t = \infty$, and $g = 0$): the underlying planar system's plasmon dispersion (blue) and the resonant wavevectors k_{nm} (red dashed) dictate resonant frequencies ω_{nm} . ω_p and k_p denote the plasma frequency and $k_p = \omega_p/c$ (c being speed of light). (c) Resonant wavelengths of the (1,1) and (2,1) (E_z profiles shown in i and ii, respectively) modes versus cylinder radius r , as predicted by eq 1 (solid lines) and numerical computations (circles).

strong and high-efficiency scattering, but all-dielectric structures cannot reach their bounds (in most parameter regimes) for the lack of subwavelength resonances. On the other hand, by equipping dielectric nanoparticles with a subwavelength resonant mechanism, achieved by coupling to a metallic substrate, these high limits may actually be approached.

We compare scattering by three types of resonators—(i) a free-space, all-dielectric resonator, (ii) a hybrid dielectric-on-metal resonator, and (iii) a metal-on-metal resonator—at a 700 nm wavelength. For each resonator, the dielectric is Si. The free-space dielectric resonator (Figure 3a) is designed to achieve superscattering⁵⁷ (Supporting Information S2), with $\eta \approx 96\%$, via aligned electric- and magnetic-dipole moments. The hybrid silicon-on-silver resonator (Figure 3b) is optimized to have a similar scattering cross-section, which is achieved in roughly one-fifth of the volume and with $\eta \approx 93\%$. Finally, the radius of the Ag-on-Ag resonator (Figure 3c) is optimized by radius (cylinder height and gap size same as Figure 3b for constant I_{inc}); notably, it only achieves only $\approx 17\%$ radiative efficiency. Figure 3d compares the scattering strengths of the three architectures, measured by σ_{sca}/V , clearly showing the dielectric–metal structure's advantage, which remains compelling across visible frequencies (Figure 3e). Figure 3e compares FOM_{sca} of different structures and includes corresponding bounds (shaded regions) based on the cylinder height (Supporting Information S3) due to the oscillatory incident fields in the presence of the reflective film. Different from Figure 3a–d, all cross sections in Figure 3e (except the dashed line) isolate both the radiative and absorptive contributions of the nanoparticles from that of the underlying film: specifically, the nanoparticles define the scattering bodies while the substrates modify their environment and are incorporated into the definitions of the incident field (Supporting Information S4). This separation isolates the scattering properties of the nanoparticle and is essential for many relevant applications. For example, to design nanoparticle scatterers for maximum light trapping in solar absorbers,^{53,54} it is crucial for the particles to have high radiative efficiency, whereas the absorber should operate in the opposite regime. At longer wavelengths, the scattering strength of the Si cylinder (blue solid line) approaches its bound, the highest among all bounds. By replacing the cylinder with a horizontally aligned nanorod in the dielectric–metal system, scattering bounds can be saturated across the entire visible spectrum (SI Figure S1). Including film

absorption and scattering in the dielectric–metal structure (blue dashed line), the hybrid resonance retains large FOM_{sca} , still outperforming all-metal and all-dielectric resonators.

The hybrid resonators have two key advantages over all-dielectric resonators, beyond the FOM_{sca} comparison in Figure 3e. First, the hybrid resonators have tunable radiative efficiencies with commensurate tunability in their scattering strengths: for instance, if an application requires 80% efficiency instead of 90%, the hybrid structure can be tuned to 80% radiative-efficiency mark while simultaneously gaining a factor of 2 in scattering per volume (σ_{sca}/V). In contrast, no such trade-off mechanism is effective in purely dielectric structures. Second, while FOM_{sca} of eq 2 neatly captures the advantages of simultaneously large scattering strength and large radiative efficiency, it may overemphasize the relative importance of near-unity radiative efficiencies. For many applications, the $\approx 93\%$ radiative efficiency of the hybrid structure as shown in Figure 3b is practically equivalent to the $\approx 96\%$ radiative efficiency of the all-silicon structure of Figure 3a, and yet this modest difference translates into a factor of 2 relative reduction in FOM_{sca} as a consequence of the $\propto 1/(1 - \eta)$ dependence of FOM_{sca} . For $\eta \sim 1$, this dependence likely overstates the comparative benefits of radiative efficiency for most applications, skewing the assessment of the comparative benefits of all-dielectric resonators. In the following section, we translate this large-response, high-radiative-efficiency capability from the far field to the near field.

Near-Field Emission Enhancements. Plasmonic losses are particularly acute in the near field, for sources in close proximity to the resonator, as the source readily accesses lossy channels that dissipate energy before it can escape into a propagating far-field photon or guided plasmon. In contrast, with negligible local dissipation, dielectric–metal resonances can provide high-Purcell, high-efficiency, and high-directionality spontaneous emission enhancements. A Purcell factor >5000 with quantum efficiency (including both photon and plasmon emission) $>90\%$ can be achieved in the optical regime. Whereas some previous work (e.g., ref 23) has not distinguished between emission into guided plasmons and emission into radiating photons, we separate each contribution and show that a simple geometrical reconfiguration (increasing/reducing the metal-film thickness) can swing the emission rate from plasmon-dominant ($>75\%$) to photon-dominant ($>75\%$) or vice versa. Directional

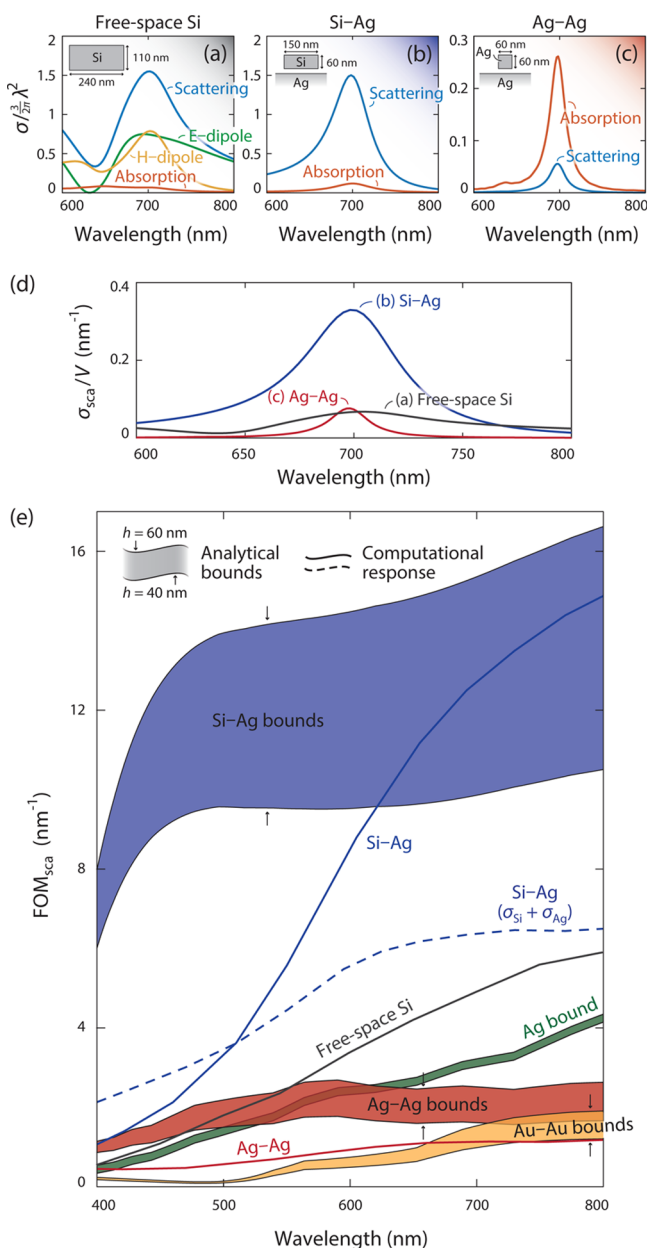


Figure 3. Dielectric–metal resonances offer strong scattering accompanied by modest absorption, at combined rates that cannot be achieved by all-metal or all-dielectric structures. Top: Scattering and absorption cross sections of nanoparticles under varying material and environment composition: (a) Si cylinder in free-space; (b–c) Si and Ag cylinders, respectively, above a semi-infinite Ag substrate with gap thickness $g = 2$ nm. Geometrical parameters (insets) are chosen to align their resonant wavelengths at 700 nm. The three structures are all illuminated by normally incident plane waves. In b–c, the absorption includes the dissipation in both the particle and the substrate. (d) The dielectric–metal structure shows the highest per-volume scattering cross-section, because it simultaneously achieves large scattering cross-section σ_{sca} , high radiative efficiency η , and a small particle volume V . (e) In the visible regime, the scattering capabilities of metal–metal geometries (Ag–Ag and Au–Au bounds), free-space metallic (Ag bound), and free-space dielectric (Si free-space) scatterers all fall short when compared with the dielectric–metal (Si–Ag) scatterer, which also approaches its own upper bound, per eq 2. For the Si–Ag and Ag–Ag structures, the gap size is fixed at 5 nm; the cylinder (both Si and Ag) height h ranges from 40 to 60 nm in order to tune the resonant wavelength.

photon and plasmon emission can also be realized via high-order resonances.

We first demonstrate *photon* emission enhancement with a silicon cylinder on a semi-infinite Ag substrate, separated by a 2 nm gap (Figure 4a). Planar dispersion analysis (SI Figure S2) suggests that this geometry should provide similar Purcell enhancement, and much higher quantum efficiency, as compared to a 5 nm-gap-size metal–metal structure. We decompose⁵⁸ the enhanced emission from a z-oriented dipole into far-field photon, guided plasmon, and local dissipative channels and obtain corresponding efficiencies (Supporting Information S7) (Figure 4b). The (1,1) and (1,2) modes achieve Purcell factors (total enhancement) > 5000 and $> 10^4$, respectively. As importantly, the (1,1) mode exhibits $> 90\%$ quantum efficiency and $> 75\%$ photon efficiency. Similar efficiencies are achieved for emitters located throughout the gap region (not shown; adopting the approach in²⁵). In the far field (Figure 4c), the (1,1) mode exhibits wide-angle emission, while the (1,2) mode enables highly directional photon emission, without the Yagi–Uda configuration^{26,59} or a periodic lattice.⁶⁰

Even higher quantum efficiencies, with similar enhancements, are possible with alternative low-loss dielectric materials (on Ag). AlSb⁶¹ nanoparticles offer close-to-unity efficiencies below their 2.2 eV direct bandgap. Ge nanoparticles exhibit Purcell factors of 2×10^4 with high radiative ($\approx 95\%$) and photon ($\approx 85\%$) efficiencies at the technologically relevant $1.55 \mu\text{m}$ wavelength (SI Figure S3). Relative to a previously proposed²⁰ infrared antenna with similar efficiency, this Purcell factor is 10 times higher.

We further demonstrate *plasmon* generation⁶² with high efficiency by using an optically thin ($t = 5$ nm) metal layer (Figure 4d). The thin metal improves the modal overlap between the gap and propagating plasmons.²⁵ The Purcell factors exceed 10^4 for all of the modes in Figure 4e. Similar to the thick-metal case, high total quantum efficiencies are achieved, with that of the (1,1) mode still $> 90\%$. Contrary to the thick-metal case, photon emission is suppressed while plasmon emission is strongly boosted: the plasmon efficiency exceeds 60% for each of the (1,1), (1,2), and (1,3) modes. The guided-plasmon propagation pattern (Figure 4f) reveals highly directional plasmon launching.

The use of ultrathin metallic films is crucial to efficient plasmon generation due to the mode-overlap improvement between the gap and propagating plasmons.²⁵ It is similarly important for the material quality of the film to remain high at such nanometric thicknesses. Recent progress in thin-film synthesis, via low-temperature slow-speed ($\approx 1 \text{ Å/min}$) epitaxial growth⁶³ demonstrated the feasibility of fabricating pristine metallic films at ever-smaller thicknesses. Conversely, the choice of semi-infinite thickness for the substrates considered in this section for enhanced photon emission, and throughout the paper for near- and far-field enhancements, is primarily for simplicity and conceptual clarity. In practice, the behavior of the resonator will be nearly identical for any film with a thickness exceeding silver's skin depth, $\gtrsim 30$ nm; the substrate thickness can consequently be adapted as necessary for different experimental techniques or practical applications.

Widely Varying Quality Factors. The quasistatic properties of metals⁷ limit the quality factors of conventional plasmonic resonances (typically < 100 in the optical regime), imposing severe restrictions on many plasmonic applications. In contrast, dielectric–metal resonances provide control over the

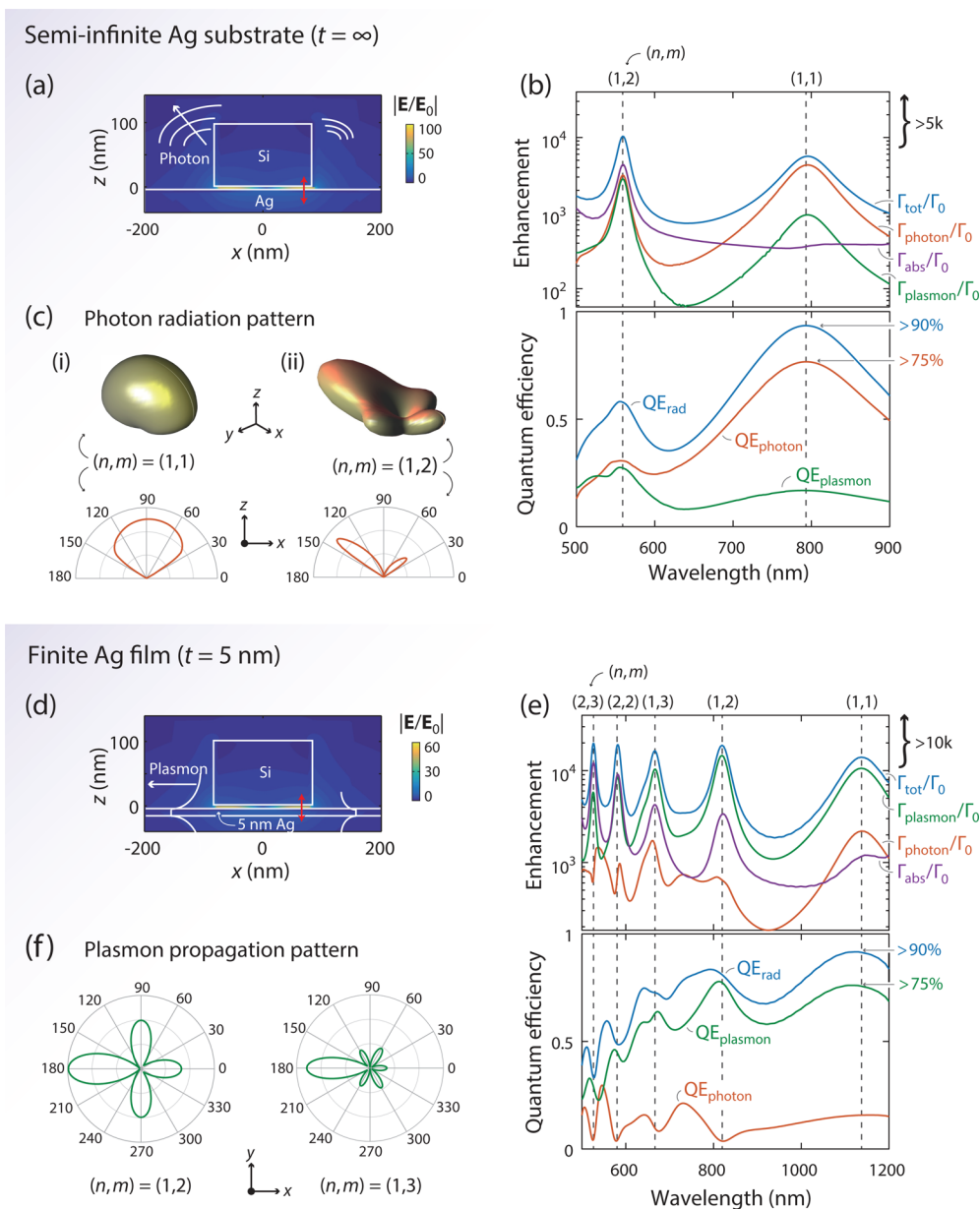


Figure 4. High-Purcell, high-efficiency, high-directionality spontaneous emission enhancement with the hybrid resonances. (a) Structure and its $(1,1)$ modal profile for photon emission. An $r = 80$ nm, $h = 100$ nm silicon cylinder above semi-infinite Ag with a $g = 2$ nm gap. A z-oriented dipole (red arrow) is located in the middle of the gap and at $x = 67$ nm. (b) Enhancement decomposition reveals strong and efficient photon emission. A high quantum efficiency $>90\%$ and photon efficiency $>75\%$ are achieved using the $(1,1)$ mode. (c) Far-field photon radiation pattern of the $(1,1)$ and $(1,2)$ mode. Highly directional photon emission is achieved using the $(1,2)$ mode. (d) Structure and its $(1,1)$ resonance profile for plasmon emission. A finite-thickness ($t = 5$ nm) metallic film is considered; all other parameters mirror those in panel a. (e) Enhancement decomposition reveals strong and efficient plasmon launching. The $(1,1)$ mode achieves a total radiative efficiency $>90\%$ and a plasmon efficiency $>75\%$. (f) Directional plasmon propagation with the $(1,2)$ and $(1,3)$ modes.

individual absorptive- and radiative-loss rates, providing options along the entire continuum between the all-metal and all-dielectric extremes.

Using approximately lossless dielectrics, such as TiO_2 at visible frequencies, plasmonic modes with extraordinarily high quality factors can be designed (Figure 5). As evidenced by their field patterns (Figure 5a–b), the modes of the dielectric–metal resonator partition into dielectric-like and plasmonic-like resonances—both of which display strong field confinement within the gap. Figure 5c shows the total, radiative, and absorptive quality factors (Q_{tot} , Q_{rad} , and Q_{abs}) of the resonances (Supporting Information S8). The dielectric-like

modes generally have higher Q_{abs} than the plasmonic-like modes because of their larger field intensity in the interior of the dielectric (Figure 5a). Unlike conventional plasmonic modes, for which Q_{tot} is mainly limited by material loss, here Q_{tot} is primarily limited by radiation loss, which can be readily tailored via the nanoparticle geometry and size. The Q_{tot} of these resonances ranges widely from ~ 10 to $\sim 10^3$, offering a wide, continuous design space for narrow- or broad-band plasmonic applications.

Robustness to Plasmonic Quantum Corrections. Quantum phenomena beyond the classical description set the ultimate limitations on the achievable response in plasmonic

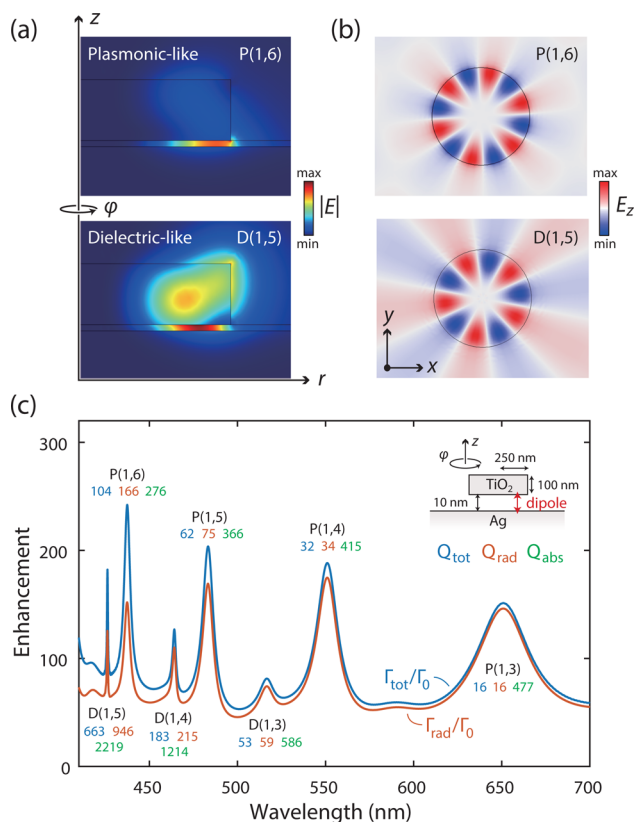


Figure 5. Low- and high-order (whispering-gallery-like) hybrid resonances offer a large continuous design space for plasmonic quality factors. (a–b) Field profiles of the plasmonic-like $[P(1,6)]$ and dielectric-like $[D(1,5)]$ resonances in the (a) r - z and (b) x - y planes. E_z are evaluated in the middle of the gap (particle) for the plasmonic-like (dielectric-like) resonance. (c) Total (blue), radiative (red), and absorptive (green) quality factors of the hybrid resonances. Inset: structure and dipole excitation for quality-factor extraction.

nanostuctures. Chief among these phenomena are nonlocality, spill-out, and surface-enabled damping.²⁸ In Ag, their joint impacts are well-described by a nonlocal, effective model—GNOR³⁷ (Supporting Information S9), a convective-diffusive hydrodynamic model—causing spectral blueshifting and broadening in structures with nanoscale features. In comparison, analogous quantum corrections in dielectrics are negligible due to the absence of free carriers. We show here that the dielectric–metal resonances display increased robustness to these detrimental quantum corrections compared to their metal–metal counterparts; taking field enhancement as a measure, the former is even superior for gaps $\lesssim 5$ nm.

Figure 6 examines these quantum corrections for 2–10 nm gap sizes, where intersurface electron tunneling is absent.²⁹ For both dielectric–metal and metal–metal structures (with equal nonlocal resonant frequencies), the resonant wavelength, quality factor, and field enhancement of the (1,1) resonance are shown (Figure 6a–c) as functions of gap size. Relative to local, classical predictions, both configurations exhibit blue-shifted resonant wavelengths and reductions in quality factor and field enhancement—all of which increase as the gap size decreases. Crucially, the metal–metal system suffers more severe reductions than its counterpart. This observation can be attributed to two cooperating effects: first, in light of the plasmon–Bessel framework laid out above (Figure 2), the planar multilayer equivalent approximately dictates the gap-

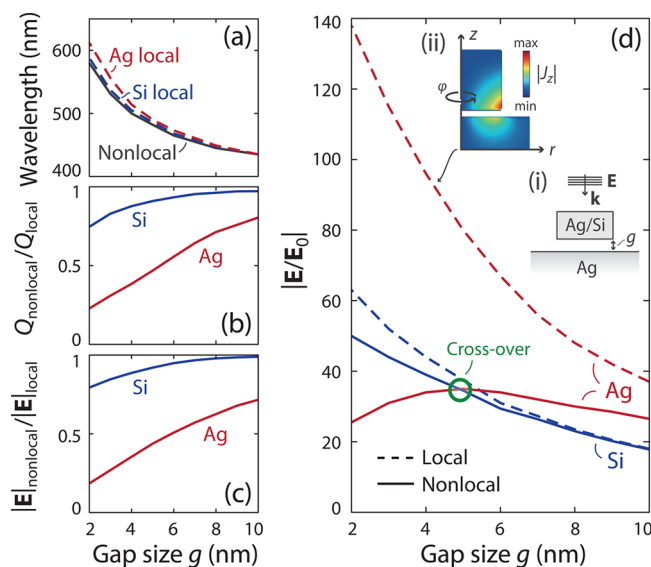


Figure 6. Hybrid resonances show increased robustness to the detrimental effects of quantum corrections than their metal–metal counterparts. The (1,1) resonances of Ag or Si nanocylinders above a semi-infinite Ag film, separated by a finite gap (inset i). The radius (height) of the Si cylinder is 50 nm (40 nm). The Ag cylinder is of identical height but of variable radius, 24–34 nm, to spectrally align the distinct structures' (nonlocal) resonance wavelength. An effective nonlocal model³⁷ reveals that (a) spectral blueshifting, (b) linewidth broadening, and (c) field enhancement (at gap center) reduction, relative to classical (local) predictions, are greatly mitigated in the hybrid resonators relative to metal–metal resonators. (d) Accounting for nonlocal response, hybrid resonances exhibit higher field enhancement than the metal–metal resonance for gap sizes $\lesssim 5$ nm (crossover in green marker). Inset ii, the induced current distribution, $|J_z|$, of the metal–metal resonance (gap, $g = 4$ nm).

dependent impact of quantum corrections. Accordingly, since the surface plasmon of the planar metal–dielectric–metal system suffers increased impact of quantum corrections compared to the planar dielectric–metal system [by a factor $1 + e^{-kg}$ (ref 31 and see SI Figure S5)], the metal–metal nanoparticle's performance is similarly reduced. Second, the metal nanoparticle's edges host sharply varying current densities (Figure 6d, inset ii) and consequently incur large nonlocal corrections in these regions.

Strikingly, the relative robustness of the hybrid resonances to quantum corrections enables them to demonstrate larger *absolute* field enhancements, for equal gap sizes $\lesssim 5$ nm (Figure 6d), than the high-intensity, pure-plasmonic metal–metal resonators. The enhancement in the latter system deteriorates drastically at these gap sizes, due to the above-noted distinguishing aspects. The comparative robustness of the hybrid resonances suggests a pathway to stronger light–matter interactions in extreme nanoscale gaps.⁶⁴

Discussion. In this Letter, we have shown the possibility for low-loss plasmonics by coupling low-loss dielectric nanoparticles with high-confinement metallic substrates. The hybrid dielectric–metal resonances exhibit strong and efficient scattering and near-field emission enhancements, large quality factors, and nonlocal robustness beyond those of conventional plasmonic nanostructures. The combined advantages of high-confinement and near-unity radiative efficiency make the hybrid platform an ideal candidate for a broad range of plasmonic

applications, such as fluorescence,⁶⁵ photovoltaics,^{53,54} sensing,⁶⁶ and metasurfaces.⁶⁷

By avoiding any structured metallic components, the architecture has practical fabrication advantages. Single- or polycrystalline metallic films exhibit much lower losses^{63,68} than metallic nanoparticles (which are typically amorphous, with more severe surface roughness). Moreover, this approach avoids the use of any metallic corners or tips that may strongly absorb due to fabrication imperfections. The dielectric particles considered here can be synthesized in colloidal form⁶⁹ and subsequently deposited or, alternatively, can be lithographically defined in situ.⁷⁰

The approach to high efficiency presented here can work in tandem with future material improvements. Just as we have shown that rearchitecting common materials can improve their plasmonic response, new, low-loss materials should be integrated into these hybrid geometries rather than conventional all-metal structures. Graphene sheets behave optically very much like ultrathin metallic films, and thus our approach extends to dielectric-on-graphene architectures for efficient graphene plasmon confinement.

Looking forward, the dielectric–metal approach prompts two directions for new exploration. First, the strong emission enhancement of the dielectric–metal resonances rely on the high index contrast between the dielectric scatterer and the dielectric spacer (comprising the gap). When the index contrast is reduced, the high efficiencies can be maintained though at the expense of reduced optical confinement. Thus, continued development of very-low-index ($n \approx 1$) materials, such as low-index SiO₂,⁷¹ aerogels,⁷² and low-index polymers,⁷³ would further increase enhancements and improve efficiencies. Second, quantum effects in dielectric and dielectric–metal structures at few-nanometer length scales are of increasing interest and should be explored further with alternative (e.g., time-dependent density functional theory) electronic and optical models. The prospect of dielectric–metal structures that are robust to deleterious nonlocal effects is especially enticing for the growing field of quantum plasmonics.⁷⁴

■ ASSOCIATED CONTENT

Supporting Information

The Supporting Information is available free of charge on the ACS Publications website at DOI: 10.1021/acs.nanolett.7b00852.

Bulk material parameters; spherical harmonics decomposition; scattering upper bound for a scatterer near a substrate; scattering and absorption of the entire particle-substrate system and of the particle alone; bound-saturated scattering realized via silicon nanorod on a silver film; confinement and dissipative loss of dielectric–dielectric–metal (DDM) and metal–dielectric–metal (MDM) waveguides; decomposition and far-field patterns of plasmon and photon emission; quality factor decomposition; generalized nonlocal optical response (PDF)

■ AUTHOR INFORMATION

Corresponding Authors

*E-mail: yyi@mit.edu.

*E-mail: owen.miller@yale.edu.

ORCID

Yi Yang: 0000-0003-2879-4968

Notes

The authors declare no competing financial interest.

■ ACKNOWLEDGMENTS

The authors thank Prof. Koppens and Dr. Bo Zhen for fruitful discussions. This work was partly supported by the Army Research Office through the Institute for Soldier Nanotechnologies under contract no. W911NF-13-D-0001. Y.Y. was partly supported by the MRSEC Program of the National Science Foundation under grant no. DMR-1419807. O.D.M. was supported by the Air Force Office of Scientific Research under award number FA9550-17-1-0093. T.C. was supported by the Danish Council for Independent Research (grant no. DFFC6108-00667). M.S. was partly supported (reading and analysis of the manuscript) by S3TEC, an Energy Frontier Research Center funded by the U.S. Department of Energy under grant no. DE-SC0001299.

■ REFERENCES

- (1) Novotny, L.; Van Hulst, N. *Nat. Photonics* **2011**, *5*, 83–90.
- (2) Giannini, V.; Fernández-Domínguez, A. I.; Heck, S. C.; Maier, S. A. *Chem. Rev.* **2011**, *111*, 3888–3912.
- (3) Biagioni, P.; Huang, J.-S.; Hecht, B. *Rep. Prog. Phys.* **2012**, *75*, 024402.
- (4) Tsakmakidis, K. L.; Boyd, R. W.; Yablonovitch, E.; Zhang, X. *Opt. Express* **2016**, *24*, 17916–17927.
- (5) Kern, J.; Kullock, R.; Prangma, J.; Emmerling, M.; Kamp, M.; Hecht, B. *Nat. Photonics* **2015**, *9*, 582–586.
- (6) Celebrano, M.; Wu, X.; Baselli, M.; Großmann, S.; Biagioni, P.; Locatelli, A.; De Angelis, C.; Cerullo, G.; Osellame, R.; Hecht, B.; Duò, L.; Ciccacci, F.; Finazzi, M. *Nat. Nanotechnol.* **2015**, *10*, 412–417.
- (7) Wang, F.; Shen, Y. R. *Phys. Rev. Lett.* **2006**, *97*, 206806.
- (8) Shahbazy, T. V. *Phys. Rev. Lett.* **2016**, *117*, 207401.
- (9) Miller, O. D.; Hsu, C. W.; Reid, M. T. H.; Qiu, W.; DeLacy, B. G.; Joannopoulos, J. D.; Soljačić, M.; Johnson, S. G. *Phys. Rev. Lett.* **2014**, *112*, 123903.
- (10) Miller, O. D.; Polimeridis, A. G.; Reid, M. H.; Hsu, C. W.; DeLacy, B. G.; Joannopoulos, J. D.; Soljačić, M.; Johnson, S. G. *Opt. Express* **2016**, *24*, 3329–3364.
- (11) Miller, O. D.; Johnson, S. G.; Rodriguez, A. W. *Phys. Rev. Lett.* **2015**, *115*, 204302.
- (12) Krasnok, A. E.; Miroshnichenko, A. E.; Belov, P. A.; Kivshar, Y. S. *Opt. Express* **2012**, *20*, 20599–20604.
- (13) Fu, Y. H.; Kuznetsov, A. I.; Miroshnichenko, A. E.; Yu, Y. F.; Luk'yanchuk, B. *Nat. Commun.* **2013**, *4*, 1527.
- (14) Kuznetsov, A. I.; Miroshnichenko, A. E.; Brongersma, M. L.; Kivshar, Y. S.; Luk'yanchuk, B. *Science* **2016**, *354*, 846.
- (15) Jahani, S.; Jacob, Z. *Nat. Nanotechnol.* **2016**, *11*, 23–36.
- (16) Khurgin, J. B. *Nat. Nanotechnol.* **2015**, *10*, 2–6.
- (17) Tassin, P.; Koschny, T.; Kafesaki, M.; Soukoulis, C. M. *Nat. Photonics* **2012**, *6*, 259–264.
- (18) Boltasseva, A.; Atwater, H. A. *Science* **2011**, *331*, 290–291.
- (19) Naik, G. V.; Shalae, V. M.; Boltasseva, A. *Adv. Mater.* **2013**, *25*, 3264–3294.
- (20) Rogobete, L.; Kaminski, F.; Agio, M.; Sandoghdar, V. *Opt. Lett.* **2007**, *32*, 1623–1625.
- (21) Kinkhabwala, A.; Yu, Z.; Fan, S.; Avlasevich, Y.; Müllen, K.; Moerner, W. *Nat. Photonics* **2009**, *3*, 654–657.
- (22) Russell, K. J.; Liu, T.-L.; Cui, S.; Hu, E. L. *Nat. Photonics* **2012**, *6*, 459–462.
- (23) Akselrod, G. M.; Argyropoulos, C.; Hoang, T. B.; Ciraci, C.; Fang, C.; Huang, J.; Smith, D. R.; Mikkelsen, M. H. *Nat. Photonics* **2014**, *8*, 835–840.
- (24) Eggleston, M. S.; Messer, K.; Zhang, L.; Yablonovitch, E.; Wu, M. C. *Proc. Natl. Acad. Sci. U. S. A.* **2015**, *112*, 1704–1709.
- (25) Yang, Y.; Zhen, B.; Hsu, C. W.; Miller, O. D.; Joannopoulos, J. D.; Soljačić, M. *Nano Lett.* **2016**, *16*, 4110–4117.

- (26) Devilez, A.; Stout, B.; Bonod, N. *ACS Nano* **2010**, *4*, 3390–3396.
- (27) Rusak, E.; Staude, I.; Decker, M.; Sautter, J.; Miroshnichenko, A. E.; Powell, D. A.; Neshev, D. N.; Kivshar, Y. S. *Appl. Phys. Lett.* **2014**, *105*, 221109.
- (28) Feibelman, P. J. *Prog. Surf. Sci.* **1982**, *12*, 287–407.
- (29) Zhu, W.; Esteban, R.; Borisov, A. G.; Baumberg, J. J.; Nordlander, P.; Lezec, H. J.; Aizpurua, J.; Crozier, K. B. *Nat. Commun.* **2016**, *7*, 11495.
- (30) Varas, A.; García-González, P.; Feist, J.; García-Vidal, F. J.; Rubio, A. *Nanophotonics* **2016**, *5*, 409.
- (31) Christensen, T.; Yan, W.; Jauho, A.-P.; Soljačić, M.; Mortensen, N. A. *Phys. Rev. Lett.* **2017**, *118*, 157402.
- (32) Esteban, R.; Borisov, A. G.; Nordlander, P.; Aizpurua, J. *Nat. Commun.* **2012**, *3*, 825.
- (33) Savage, K. J.; Hawkeye, M. M.; Esteban, R.; Borisov, A. G.; Aizpurua, J.; Baumberg, J. J. *Nature* **2012**, *491*, 574–577.
- (34) Scholl, J. A.; García-Etxarri, A.; Koh, A. L.; Dionne, J. A. *Nano Lett.* **2013**, *13*, 564–569.
- (35) García de Abajo, F. J. *J. Phys. Chem. C* **2008**, *112*, 17983–17987.
- (36) Ciraci, C.; Hill, R.; Mock, J.; Urzhumov, Y.; Fernández-Domínguez, A.; Maier, S.; Pendry, J.; Chilkoti, A.; Smith, D. *Science* **2012**, *337*, 1072–1074.
- (37) Mortensen, N. A.; Raza, S.; Wubs, M.; Søndergaard, T.; Bozhevolnyi, S. I. *Nat. Commun.* **2014**, *5*, 3809.
- (38) West, P. R.; Ishii, S.; Naik, G. V.; Emani, N. K.; Shalae, V. M.; Boltasseva, A. *Laser Photonics Rev.* **2010**, *4*, 795–808.
- (39) Khurgin, J. B. *Philos. Trans. R. Soc., A* **2017**, *375*, 20160068.
- (40) Ammari, H.; Ciraolo, G.; Kang, H.; Lee, H.; Milton, G. W. *Arch. Ration. Mech. Anal.* **2013**, *208*, 667–692.
- (41) Khurgin, J. B.; Sun, G. *Appl. Phys. Lett.* **2010**, *96*, 181102.
- (42) Zayats, A. V.; Maier, S. A. *Active plasmonics and tuneable plasmonic metamaterials*; Wiley Online Library, 2013.
- (43) Raman, A.; Shin, W.; Fan, S. *Phys. Rev. Lett.* **2013**, *110*, 183901.
- (44) Khurgin, J. B.; Boltasseva, A. *MRS Bull.* **2012**, *37*, 768–779.
- (45) Oulton, R. F.; Sorger, V. J.; Genov, D.; Pile, D.; Zhang, X. *Nat. Photonics* **2008**, *2*, 496–500.
- (46) Esteban, R.; Teperik, T.; Greffet, J.-J. *Phys. Rev. Lett.* **2010**, *104*, 026802.
- (47) Moreau, A.; Ciraci, C.; Mock, J. J.; Hill, R. T.; Wang, Q.; Wiley, B. J.; Chilkoti, A.; Smith, A. *Nature* **2012**, *492*, 86–89.
- (48) Belacel, C.; Habert, B.; Bigourdan, F.; Marquier, F.; Hugonin, J.-P.; de Vasconcellos, S. M.; Lafosse, X.; Coolen, L.; Schwob, C.; Javaux, C.; Dubertret, B.; Greffet, J.-J.; Senellart, P.; Maitre, A. *Nano Lett.* **2013**, *13*, 1516–1521.
- (49) Rose, A.; Hoang, T. B.; McGuire, F.; Mock, J. J.; Ciraci, C.; Smith, D. R.; Mikkelsen, M. H. *Nano Lett.* **2014**, *14*, 4797–4802.
- (50) Faggiani, R.; Yang, J.; Lalanne, P. *ACS Photonics* **2015**, *2*, 1739–1744.
- (51) Bowen, P. T.; Smith, D. R. *Phys. Rev. B: Condens. Matter Mater. Phys.* **2014**, *90*, 195402.
- (52) Gordon, R. *Phys. Rev. B: Condens. Matter Mater. Phys.* **2006**, *73*, 153405.
- (53) Atwater, H. A.; Polman, A. *Nat. Mater.* **2010**, *9*, 205–213.
- (54) Brongersma, M. L.; Cui, Y.; Fan, S. *Nat. Mater.* **2014**, *13*, 451–460.
- (55) Gustafsson, M.; Sohl, C.; Kristensson, G. *Proc. R. Soc. London, Ser. A* **2007**, *463*, 2589–2607.
- (56) Hugonin, J.-P.; Besbes, M.; Ben-Abdallah, P. *Phys. Rev. B: Condens. Matter Mater. Phys.* **2015**, *91*, 180202.
- (57) Ruan, Z.; Fan, S. *Phys. Rev. Lett.* **2010**, *105*, 013901.
- (58) Yang, J.; Hugonin, J.-P.; Lalanne, P. *ACS Photonics* **2016**, *3*, 395–402.
- (59) Curto, A. G.; Volpe, G.; Taminiau, T. H.; Kreuzer, M. P.; Quidant, R.; van Hulst, N. F. *Science* **2010**, *329*, 930–933.
- (60) Lozano, G.; Louwers, D. J.; Rodríguez, S. R.; Murai, S.; Jansen, O. T.; Verschuuren, M. A.; Rivas, J. G. *Light: Sci. Appl.* **2013**, *2*, e66.
- (61) Zollner, S.; Lin, C.; Schönherr, E.; Böhringer, A.; Cardona, M. J. *Appl. Phys.* **1989**, *66*, 383–387.
- (62) Gan, C. H.; Hugonin, J.-P.; Lalanne, P. *Phys. Rev. X* **2012**, *2*, 021008.
- (63) Wu, Y.; Zhang, C.; Estakhri, N. M.; Zhao, Y.; Kim, J.; Zhang, M.; Liu, X.-X.; Pribil, G. K.; Alù, A.; Shih, C.-K.; Li, X. *Adv. Mater.* **2014**, *26*, 6106–6110.
- (64) Chikkaraddy, R.; de Nijs, B.; Benz, F.; Barrow, S. J.; Scherman, O. A.; Rosta, E.; Demetriadou, A.; Fox, P.; Hess, O.; Baumberg, J. J. *Nature* **2016**, *535*, 127–130.
- (65) Tam, F.; Goodrich, G. P.; Johnson, B. R.; Halas, N. J. *Nano Lett.* **2007**, *7*, 496–501.
- (66) Anker, J. N.; Hall, W. P.; Lyandres, O.; Shah, N. C.; Zhao, J.; Van Duyne, R. P. *Nat. Mater.* **2008**, *7*, 442–453.
- (67) Huang, L.; Chen, X.; Mühlender, H.; Zhang, H.; Chen, S.; Bai, B.; Tan, Q.; Jin, G.; Cheah, K.-W.; Qiu, C.-W.; Li, J.; Zentgraf, T.; Zhang, S. *Nat. Commun.* **2013**, *4*, 2808.
- (68) McPeak, K. M.; Jayanti, S. V.; Kress, S. J.; Meyer, S.; Iotti, S.; Rossinelli, A.; Norris, D. J. *ACS Photonics* **2015**, *2*, 326–333.
- (69) Fojtik, A.; Henglein, A. *Chem. Phys. Lett.* **1994**, *221*, 363–367.
- (70) Person, S.; Jain, M.; Lapin, Z.; Sáenz, J.; Wicks, G.; Novotny, L. *Nano Lett.* **2013**, *13*, 1806–1809.
- (71) Xi, J.-Q.; Schubert, M. F.; Kim, J. K.; Schubert, E. F.; Chen, M.; Lin, S.-Y.; Liu, W.; Smart, J. A. *Nat. Photonics* **2007**, *1*, 176–179.
- (72) Sun, Y.; Forrest, S. R. *Nat. Photonics* **2008**, *2*, 483–487.
- (73) Groh, W.; Zimmermann, A. *Macromolecules* **1991**, *24*, 6660–6663.
- (74) Fitzgerald, J. M.; Narang, P.; Craster, R. V.; Maier, S. A.; Giannini, V. *Proc. IEEE* **2016**, 1–16.